J. Fluid Mech. (2009), *vol.* 639, *pp.* 373–401.
doi:10.1017/S0022112009991078

Torque reduction in Taylor–Couette flows subject to an axial pressure gradient

MARCELLO MANNA[1]† AND ANDREA VACCA[2]

[1]Dipartimento di Ingegneria Meccanica per l'Energetica, Universitá di Napoli 'Federico II', via Claudio 21, 80125 Naples, Italy

[2]Dipartimento di Ingegneria Civile, Seconda Universitá di Napoli, via Roma 29, 81031 Aversa (CE), Italy

(Received 17 September 2008; revised 2 July 2009; accepted 3 July 2009; first published online 13 October 2009)

The paper investigates the phenomena occurring in a Taylor–Couette flow system subject to a steady axial pressure gradient in a small envelope of the Taylor–Reynolds state space under transitional regimes. A remarkable net power reduction necessary to simultaneously drive the two flows compared to that required to drive the Taylor–Couette flow alone is documented under non-trivial conditions. The energy transfer process characterizing the large-scale coherent structures is investigated by processing a set of statistically independent realizations obtained from direct numerical simulation. The analysis is conducted with an incompressible three-dimensional Navier–Stokes flow solver employing a spectral representation of the unknowns.

1. Introduction

The Taylor–Couette flow in an annulus with a fixed outer cylinder and a pressure-driven axial flow has several important engineering applications, such as those occurring in chemical engineering processes, oil well drilling technology, biological flows and turbomachinery, to name a few. Most of the available literature is focused on the stability analysis of the combined flow at critical and supercritical regimes, providing information on the characteristics of the toroidal vortices appearing in the gap. Pioneering works on the linear stability analysis for axisymmetric disturbances in a narrow annular gap are due to Chandrasekhar (1960, 1962) and di Prima (1960) and were later extended to wide annular gaps (Chung & Astill 1977; di Prima & Pridor 1979; Takeuchi & Jankowski 1981; Ng & Turner 1982). More recently nonlinear dynamics of spiral Poiseuille problem for moderate axial through flow has been investigated by numerically solving the unsteady Navier–Stokes equations (Hoffmann, Lucke & Pinter 2004; Avila, Meseguer & Marques 2006; Heise *et al.* 2008).

The above theoretical analysis, together with several experimental investigations (Snyder 1962; Schwarz, Springett & Donnelly 1964; Takeuchi & Jankowski 1981; Ng & Turner 1982; Tsameret & Steinberg 1994), have shown the stabilizing effect of the axial flow towards the Couette regime, so that the critical Taylor number (Ta_c) is increased. Secondary transitions were already documented at the beginning of the 1960s by Kaye & Elgar (1958) and Becker & Kaye (1962). A few fundamental

† Email address for correspondence: marcello.manna@unina.it

studies concerning the identification of the flow regimes in an annulus with an axial flow and a rotating inner cylinder have been carried out by Lueptow, Docter & Min (1992). Seven flow regimes have been identified in the Taylor–Reynolds numbers (Ta–Re) plane for a wide range of Taylor numbers and moderate axial Reynolds numbers. Wereley & Lueptow (1999) used two-dimensional time-resolved velocity measurements to investigate the axial translation of the inter-gap vortices and furnished details of the fluid transport between them. The numerical study of Hwang & Yang (2004) supported the experiments of Wereley & Lueptow (1999) and provided additional details about the vortex dynamics. Experimental and numerical studies of the combined flow at high Reynolds numbers for wide gap geometries, providing mean velocity and Reynolds stress radial distributions, can be found in Nouri & Whitelaw (1994), Escudier & Gouldson (1995), Chung & Sung (2005) and Jung & Sung (2006). More applied investigations are due to Kataoka, Doi & Komai (1977) who investigated the effects of periodically varying rates of heat transfer in Taylor vortex flow with an axial flow rate in a wide gap geometry. They showed that as the axial flow is gradually increased, not only is the regular sinusoidal variation of the heat transfer coefficient distorted, but also its mean value and amplitude are greatly reduced. A map in the Taylor–Reynolds numbers plane is also provided, showing the occurrence of small secondary vortices attributed to the separation of the boundary layer from the outer cylinder wall.

While the wide gap geometry has been extensively investigated, both numerically and experimentally, the narrow one, also enjoying numerous engineering applications, is less studied. A noteworthy exception is provided by the experimental work of Yamada (1962*a*,*b*). In Yamada (1962*a*) the resistance through coaxial cylinders with a rotating inner one, has been studied for six gap sizes and various combinations of axial and rotational flows. The friction coefficient was shown to be unaffected up to a certain rotation speed when the axial flow is laminar, while beyond this speed the resistance increases. Furthermore the critical Taylor number was shown to be a non-monotonic function of the axial Reynolds number characterized by a neat maximum. Similar experiments aimed at the determination of the effects of the axial pressure gradient on the torque are reported in Yamada (1962*b*), with and without circumferential grooves on the inner cylinder surface. When grooves and axial flow are absent, the torque coefficient was shown to increase with the clearance, up to some value of the angular speed. The axial flow increases the critical Taylor number up to a certain value ($Re \sim 700$) beyond which it decreases. For a fixed Reynolds number and $Ta < Ta_c$, the torque coefficient scales like Ta^{-1}, while for $Ta > Ta_c$ it increases, reaching a maximum before starting to decrease again, eventually attaining a $Ta^{-1/4}$ slope. At constant Taylor number ($10^3 \leqslant Ta \leqslant 10^4$), the torque coefficient decreases with Reynolds number reaching a minimum, in some instances equal to the Couette value, before increasing again. In the first stage of this process the torque coefficient reduction may be accompanied by a complete suppression of the vortical structures in the clearance, through a nonlinear process. It is precisely the dynamics of the vortex suppression phenomena which has been focused on in the present paper. Field data, obtained from the numerical solution of the three-dimensional Navier–Stokes equations with a high accurate method, have been used to investigate the energy transfer process of the large-scale structures during the relaminarization.

The paper is organized as follows. The problem formulation detailing the run matrix in the plane of dimensionless governing parameters is reported in § 2, while a short introduction of the mathematical model and the numerical procedure are given in § 3. Details concerning the computational domain along with a grid convergence

study can be found in the Appendix. Finally, results in terms of global and local parameters are provided in § 4. Conclusions are given in § 5.

2. Problem formulation

The problem under investigation is the flow in an annular duct consisting of two concentric cylinders out of which the inner one rotates at constant angular velocity while the outer one is stationary. The duct is subject to a uniform steady pressure gradient generating an axial flow, which, under specific regimes, interacts to some remarkable extent with the base flow.

The geometry is completely defined by the inner radius R_i and the outer radius $R_o = R_i + S$, with S the gap width, and the duct length L_z or, equivalently, by the ratio of the inner radius to the outer radius, $\eta = R_i/R_o$, and the dimensionless axial length $\ell_z = L_z/S$.

The combined motion is governed by two dimensionless parameters, the Taylor and Reynolds numbers, defined as $Ta = \Omega R_i S/\nu$ and $Re = U_b S/\nu$, with Ω, U_b and ν the angular velocity, the axial bulk velocity and the kinematic viscosity, respectively. For $Re = 0$ and Ta smaller than a critical value Ta_c, a closed expression for the velocity distribution exists:

$$U = V = 0, \quad W(R) = \Omega R_i \frac{\eta}{1-\eta^2}\left[\frac{R_o}{R} - \frac{R}{R_o}\right], \tag{2.1}$$

U, V and W being the axial, radial and azimuthal velocity components.

When Ta exceeds Ta_c the flow becomes linearly unstable to axisymmetric three-dimensional toroidal vortices, which are usually parameterized by expanding in truncated Fourier series the velocity vector field (Davey 1965). Therefore it is customary to represent them in terms of axial and azimuthal wavenumber pairs. In the narrow gap limit ($\eta \to 1$) the critical value can be estimated by eigenvalue analysis (Chandrasekhar 1961) as

$$Ta_c = 41.41(1-\eta)^{-1/2}. \tag{2.2}$$

With further increase in the Taylor number the flow becomes again unstable beyond a second critical value ($Ta \sim 1.1\ Ta_c$) (di Prima 1961; Coles 1965; Schroeder & Keller 1990), the instability resulting in a wavy vortex flow pattern with azimuthally propagating waves superposed on the Taylor vortices (Marcus 1984). These states characterized by different axial and azimuthal wavenumbers are not a unique function of the Taylor number, since it has been experimentally demonstrated that different equilibrium states coexist on each stable bifurcation branch (Coles 1965; Moulic & Yao 1996). With further increase in the Taylor number beyond $Ta \sim 10\ Ta_c$ new regimes have been experimentally observed, namely modulated wavy vortex with a quasi-periodic feature (up to $Ta \sim 12\ Ta_c$), turbulent modulated wavy vortex (up to $Ta \sim 19\ Ta_c$), turbulent wavy vortex (up to $Ta \sim 22\ Ta_c$) and turbulent vortex (Fenstermacher, Swinney & Gollub 1979; Andereck, Liu & Swinney 1986; Lueptow, Docter & Min 1992). Those flow topologies represent a sequence of transitional states towards turbulent regimes by spectral evolution; that is to say transition is viewed as a cascade process in which energy is transferred by nonlinear interaction through a discrete spectrum to progressively higher frequencies in a two-dimensional wavenumber space. When the Taylor number approaches values of order $5-10 \times 10^4$ the discrete spectrum changes gradually to a continuous one by broadening of the initially sharp energy peaks (Coles 1965).

Superposing an axial flow changes the stability scenario, as demonstrated by both experimental (Kaye & Elgar 1958; Snyder 1962) and theoretical investigations (Chandrasekhar 1961; Chung & Astill 1977; Hasoon & Martin 1977; di Prima & Pridor 1979). More specifically, the axial flow in the annulus enlarges the stability region of the circular Couette flow, increasing the critical Taylor number as the Reynolds number of the axial flow is increased. Within the above region of the state space (Ta, Re), termed spiral Poiseuille flow (SPF; Joseph 1976), the azimuthal and axial velocity components are independent functions of the radial coordinate for given η:

$$\left.\begin{aligned} U(R) &= 2U_b \frac{(1-(R/R_o)^2)\log\eta - \log(R/R_o)(1-\eta^2)}{(1+\eta^2)\log\eta + (1-\eta^2)}, \\ V(R) &= 0, \\ W(R) &= \Omega R_i \frac{\eta}{1-\eta^2}\left[\frac{R_o}{R} - \frac{R}{R_o}\right]. \end{aligned}\right\} \tag{2.3}$$

The linear stability of the SPF has been the subject of several theoretical studies (Chandrasekhar 1960; di Prima 1960; Datta 1965; Hughes & Reid 1968; Elliott 1973), all of which relied on various approximations. More recently Recktenwald, Lucke & Muller (1993) computed the first instability, providing the coefficients of the complex Ginzburg–Landau equation for a wide range of radius ratio as a function of the through-flow strength for small Reynolds numbers. Their results have been fitted for each η and Re by a power law expansion well representing the numerical data in the the range $0 \leqslant Re \leqslant 20$ as

$$Ta_c^{SPF} = \sqrt{\frac{\eta}{1-\eta}a_0 + \left[1 + \left(\frac{Re}{a_2}\right)^2 + \left(\frac{Re}{a_4}\right)^4\right]}. \tag{2.4}$$

For $\eta = 0.975$, the closest available η value, the coefficients appearing in (2.4) are $a_0 = 1746$, $a_2 = 35.97$, $a_4 = 65.34$ (Recktenwald *et al.* 1993).

Outside the instability limit Ta_c^{SPF}, a rich variety of flow regimes can be found, each of which are characterized by boundaries whose shape can only be ascertained via carefully designed experimental tests. The occurrence of these regimes has been visually and optically studied detecting the transition over a wide range of Taylor numbers for moderate Reynolds numbers ($\eta = 0.848$, $Ta \leqslant 3000$ and $Re \leqslant 40$) by Lueptow *et al.* (1992). From our point of view, the fundamental analysis of the flow regimes in the (Ta, Re) space could prove very useful to explain certain phenomena of engineering relevance occurring in devices whose flow features are similar to those described in Lueptow *et al.* (1992). Yamada (1962*a*,*b*) experimentally addressed the resistance and torque behaviour of a water flow through coaxial cylinders characterized by narrow gap geometries ($\eta > 0.897$), for a wide range of Ta and Re. No topological information about the characterization of the flow regimes was provided. In his landmark contribution, among many interesting achievements, it was found that for a fixed Taylor number, the torque decreases as the axial flow is gradually increased, reaching a nearly constant value, while the axial pressure drop increases too. Such a behaviour is observed in a range of axial flows (i.e Reynolds numbers), beyond which both torque and axial resistance increase again. In this study we focused on specific regimes which, according to the experimental data of Yamada (1962*a*), exhibit a peculiar behaviour of the axial resistance and torque, analysing an annular duct characterized by $\eta = 0.98$. Two different Taylor numbers have been

	DNS data		Experimental data	
$Re \setminus Ta$	1000	1500	1000	1500
0	X	X	X	X
50	X	X	X	X
100	X	X	/	X
200	X	X	X	X
400	X	X	X	X

TABLE 1. Run matrix detailing Taylor and Reynolds number pairs presently investigated; DNS, direct numerical simulation.

considered, namely $Ta = 1000$ and $Ta = 1500$, for each of which a moderate axial pressure gradient has been superposed. The resulting Reynolds number, ranging from 0 to 400, is summarized in table 1.

Since the work of Lueptow *et al.* (1992) several flow regimes have been experimentally observed as the Taylor number is increased, depending on the axial flow rate. Typically the experimental studies are based on the spectral analysis of the time-dependent properties of the reflected light produced by a laser beam illuminating a small region of the outer portion of the annulus. Unfortunately no such data are available for the geometry ($\eta = 0.98$) and all state parameters presently investigated (see table 1), so that we can only rely on the computed data. Let us observe that if their results ($\eta = 0.848$) were applicable to the present case ($\eta = 0.98$), then only 2 out of 10 regimes could be defined, the $Ta = 1000$ and $Re = 0$ modulated wavy vortices (MWV) and the $Ta = 1500$ and $Re = 0$ turbulent wavy vortices (TWV). From the shape of the boundaries at $Re = 40$ given in figure 3 of Lueptow, Docter & Min (1992), the $Ta = 1500$, $Re = 50$ case could be classified as TWV with some uncertainty. To orient the reader, we present in figure 1 a schematic diagram showing in the Ta–Re plane approximate boundaries useful for the characterization of the computed regimes. The solid line defines the region in which SPF conditions were experimentally observed by Yamada (1962*a*,*b*), while the dashed line represents the stability limit (2.4) slightly extended outside its fitting range ($0 \leqslant Re \leqslant 20$).

To give an idea of the complexity of the problem under investigation, we show in figure 2, through a few instantaneous realizations, the effects of the mean flow rate on the crossflow vector field, in the $Ta = 1500$ case. The plot, presented in dimensionless coordinates ($y = (R - R_i)/S$ and $z = Z/S$), highlights the multiple-scale features of the energy-producing events as opposed to the few, large-sized, regular structures characterizing laminar helical vortex and helical wavy vortex regimes which occur at much smaller Ta, as shown in Wereley & Lueptow (1999). Thus at the current Taylor numbers the vortices appear turbulent, in agreement with the experiments of Lueptow *et al.* (1992) carried out at comparable Ta and slightly smaller η and Re.

Without entering into the details of the definition of the boundaries separating one regime from the other in a topological sense, it turns out that the volume-averaged turbulent shear stress is always comparable in magnitude with the viscous one, as detailed in § 4. Thus there is a significant scale separation requiring an appropriate spatial and temporal resolution.

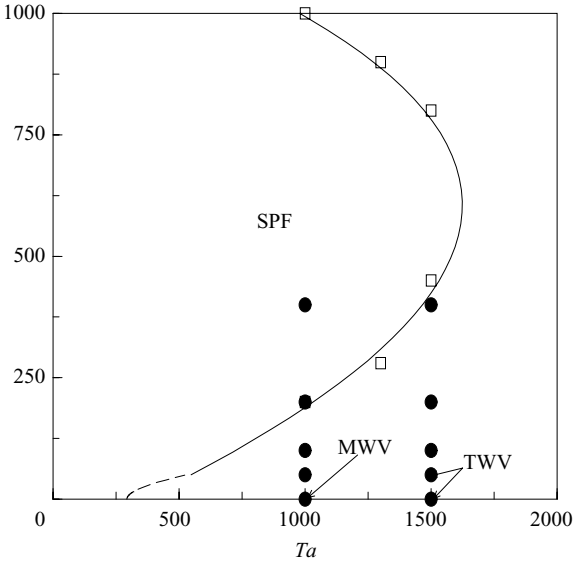

FIGURE 1. Schematic diagram in the Ta–Re plane, showing approximate boundaries between different flow regimes: dashed line, (2.4); □, experimental data in the SPF regime of Yamada (1962*a*,*b*); solid line, polynomial best fit of □; ●, computed data as defined in table 1.

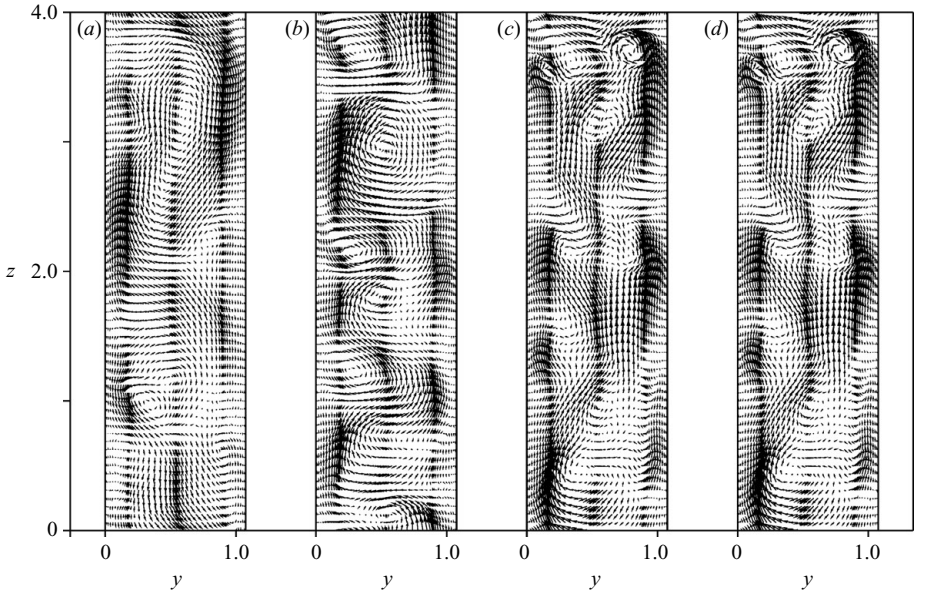

FIGURE 2. Instantaneous velocity vector fields ($Ta = 1500$) in the cross-plane: (*a*) $Re = 0$; (*b*) $Re = 50$; (*c*) $Re = 100$; (*d*) $Re = 200$.

3. Numerical method and computational set-up

The governing equations are the incompressible Navier–Stokes equations in their primitive variable dimensionless form:

$$\frac{\partial \boldsymbol{u}}{\partial t} = -\nabla p - \mathscr{N}\boldsymbol{u} + \frac{1}{Ta}\mathscr{L}\boldsymbol{u} + \mathscr{S}\boldsymbol{u} \tag{3.1}$$

and

$$\nabla \circ \boldsymbol{u} = 0, \tag{3.2}$$

where $\boldsymbol{u} = (u, v, w)^t$, with u, v and w the dimensionless axial, radial and azimuthal velocity components, and p is the dimensionless pressure. Clearly the characteristic length and velocity scales are assumed to be the gap width $R_o - R_i$ and velocity of the inner cylinder ΩR_i, respectively. The source term $\mathscr{S}$ is introduced to deal with a specific class of problems, namely flows in equilibrium in the axial direction. It therefore represents the effect of a steady pressure gradient, applied to induce an axial flow with prescribed Reynolds number Re:

$$\mathscr{S}\boldsymbol{u} = \left(\frac{\lambda}{4}\frac{Re^2}{Ta^2}, 0, 0\right)^t, \tag{3.3}$$

with λ a coefficient whose value is a unique unknown function of the Reynolds number. Owing to the nonlinear dependence of λ on the Reynolds number it is impossible to specify *a priori* the λ value corresponding to a well-defined Re. Therefore in the present study λ is iteratively computed at each time step from the axial momentum equilibrium condition, in integral form.

Equations (3.1) and (3.2) are subject to the boundary conditions $\boldsymbol{u} = (0, 0, 1)^t$ and $\boldsymbol{u} = (0, 0, 0)^t$ at the inner and outer radii, respectively.

The differential operators of (3.1) and (3.2) in cylindrical coordinates are given by

$$\left.\begin{aligned}
\nabla u &= \left(\frac{\partial u}{\partial z},\ \frac{\partial u}{\partial r},\ \frac{1}{r}\frac{\partial u}{\partial \theta}\right)^t,\\
\mathscr{N}\boldsymbol{u} &= \nabla \boldsymbol{u} \cdot \boldsymbol{u} = \left(\nabla u \cdot \boldsymbol{u},\ \nabla v \cdot \boldsymbol{u} - \frac{w n_\theta}{r},\ \nabla w \cdot \boldsymbol{u} + \frac{v n_\theta}{r}\right)^t,\\
\nabla \circ \boldsymbol{u} &= \frac{\partial u}{\partial z} + \frac{1}{r}\frac{\partial r v}{\partial r} + \frac{1}{r}\frac{\partial w}{\partial \theta},\\
\Delta u &= \frac{\partial^2 u}{\partial z^2} + \frac{1}{r}\frac{\partial}{\partial r}\left(r\frac{\partial u}{\partial r}\right) + \frac{1}{r^2}\frac{\partial^2 u}{\partial \theta^2},\\
\mathscr{L}\boldsymbol{u} &= \Delta \boldsymbol{u} = \left(\Delta u,\ \Delta v - \frac{v}{r^2} - \frac{2}{r^2}\frac{\partial w}{\partial \theta},\ \Delta w + \frac{2}{r^2}\frac{\partial v}{\partial \theta} - \frac{w}{r^2}\right)^t,\\
\nabla \times \boldsymbol{u} &= \left(\frac{1}{r}\frac{\partial r w}{\partial r} - \frac{1}{r}\frac{\partial v}{\partial \theta},\ \frac{1}{r}\frac{\partial u}{\partial \theta} - \frac{\partial w}{\partial z},\ \frac{\partial v}{\partial z} - \frac{\partial u}{\partial r}\right)^t.
\end{aligned}\right\} \tag{3.4}$$

Following the standard pressure correction approach we integrate the governing equations, decoupling the velocity and the pressure at each time step (van Kan 1986). To overcome the time step limitations of the diffusive operator we implicitly discretize the viscous terms (Crank–Nicolson); the convective operator, written in skew-symmetric form, and the source term are instead treated explicitly for simplicity (Adams–Bashforth). Let $\boldsymbol{u}^n$ be the approximation to $\boldsymbol{u}(\cdot, n\Delta t)$ at time level $n\Delta t$ and $\boldsymbol{v}$ the intermediate velocity vector field of the time-splitting method whose curl $\nabla \times \boldsymbol{v}$ approximates $\nabla \times \boldsymbol{u}$ up to $O(\Delta t^2)$. With these assumptions the semi-discrete form of (3.1) and (3.2) reads

$$\frac{\boldsymbol{v} - \boldsymbol{u}^n}{\Delta t} - \frac{1}{2Re}\Delta(\boldsymbol{v} + \boldsymbol{u}^n) = -\nabla p^n - \frac{3}{2}(\mathscr{N}\boldsymbol{u}^n - \mathscr{S}\boldsymbol{u}^n) + \frac{1}{2}(\mathscr{N}\boldsymbol{u}^{n-1} - \mathscr{S}\boldsymbol{u}^{n-1}), \tag{3.5}$$

$$\frac{\boldsymbol{u}^{n+1} - \boldsymbol{v}}{\Delta t} = -\frac{1}{2}\nabla(p^{n+1} - p^n), \tag{3.6}$$

$$\nabla \circ \boldsymbol{u}^{n+1} = 0. \tag{3.7}$$

The above formulation introduces a vortex sheet of strength $\mathcal{O}(\Delta t^2)$ at the boundaries which vanishes in the steady state.

Equations (3.5) constitute a set of coupled Helmholtz equations for the predicted velocity components; a scalar Poisson equation for the pressure follows from (3.6) and (3.7). Referring to the former set, for the sake of clarity, let us rewrite (3.5), as follows:

$$\alpha \boldsymbol{v} - \mathscr{L}\boldsymbol{v} = \boldsymbol{f}, \tag{3.8}$$

where $\alpha = 2Ta/\Delta t$ and $\boldsymbol{f}$ includes all known terms involved in (3.5). Unlike the Cartesian case, where the implicit treatment of the diffusion (together with the explicit treatment of the convection) still allows to uncouple the momentum equations, in cylindrical coordinates the radial and azimuthal momentum equations are strongly coupled, as it can be easily verified by inspection of (3.4). As described in Manna & Vacca (1999), the flow is assumed to be homogeneous in the azimuthal direction θ, and thus the computational efficiency of the fast Fourier Transform could be enjoyed by expanding in Fourier series all variables. The velocity field and the pressure can then be represented in the transformed space by M_θ complex coefficients $\boldsymbol{v}_m$ and p_m as follows:

$$\boldsymbol{v}(z, r, \theta, t) = \sum_{m=-M_\theta/2}^{M_\theta/2-1} \boldsymbol{v}_m(z, r, t)\mathrm{e}^{\mathrm{i}m\theta} \quad \forall\theta \in [0, 2\pi], \tag{3.9}$$

$$p(z, r, \theta, t) = \sum_{m=-M_\theta/2}^{M_\theta/2-1} p_m(z, r, t)\mathrm{e}^{\mathrm{i}m\theta} \quad \forall\theta \in [0, 2\pi]. \tag{3.10}$$

Introducing (3.9) in (3.8) and following the Galerkin projection method yields

$$\alpha \boldsymbol{v}_m - \hat{\mathscr{L}}\boldsymbol{v}_m = \boldsymbol{f}_m, \tag{3.11}$$

with

$$\left.\begin{aligned} \hat{\mathscr{L}}\boldsymbol{v}_m = \Bigg(& \Delta_{rz}u_m - \frac{m^2}{r^2}u_m,\ \Delta_{rz}v_m - \frac{m^2+1}{r^2}v_m \\ & - \frac{2}{r^2}\mathrm{i}\,m\ w_m,\ \Delta_{rz}w_m - \frac{m^2+1}{r^2}w_m + \frac{2}{r^2}\mathrm{i}\,m\ v_m\Bigg)^t, \\ \Delta_{rz}\cdot = & \frac{\partial^2\cdot}{\partial z^2} + \frac{1}{r}\frac{\partial}{\partial r}\left(r\frac{\partial\cdot}{\partial r}\right). \end{aligned}\right\} \tag{3.12}$$

An analogous procedure is applied to the pressure Poisson equation.

This representation provides the possibility of decoupling the diffusive terms, and thus a diagonalization of (3.12) can be obtained according to the following change of variables (Orzag & Patera 1983):

$$\tilde{\boldsymbol{v}}_m = (\tilde{u},\ \tilde{v},\ \tilde{w})^t \equiv (u_m,\ v_m + \mathrm{i}w_m,\ v_m - \mathrm{i}w_m)^t. \tag{3.13}$$

Equation (3.11) then reduces to

$$\alpha \tilde{\boldsymbol{v}}_m - \tilde{\mathscr{L}}\tilde{\boldsymbol{v}}_m = \tilde{\boldsymbol{f}}_m, \tag{3.14}$$

where the scalar components of $\tilde{\boldsymbol{f}}_m$ obey analogous transformation as (3.13), and

$$\tilde{\mathscr{L}}\tilde{\boldsymbol{v}}_m = \left(\Delta_{rz}\tilde{u} - m^2\tilde{u},\ \Delta_{rz}\tilde{v} - \frac{(m+1)^2}{r^2}\tilde{v},\ \Delta_{rz}\tilde{w} - \frac{(m-1)^2}{r^2}\tilde{w}\right)^t. \tag{3.15}$$

Irrespective of the functional representation of the unknowns in the z and r directions the above decomposition reduces, in a quite general form, the original set of partial differential equations (3.5) to a cascade of two-dimensional uncoupled elliptic problems, which do not differ from their Cartesian counterpart except for the explicit r dependence of the differential operators. Additional computational efficiency can be gained assuming periodicity in the axial direction and expanding all variables in truncated Fourier series, reducing the original set of equations to a double cascade of one-dimensional uncoupled elliptic problems. Finally, in the inhomogeneous (radial) direction r a Chebyshev polynomial expansion is adopted and a multi-domain patching collocation method applied to efficiently solve the resulting equations. Using a linearity argument the elliptic problem is decomposed in a set of decoupled inhomogeneous problems within each subdomain. The continuity of the solution and its normal derivative along the interfaces is enforced seeking the appropriate harmonic extension. While the inhomogeneous problems are solved with standard Chebyshev collocation algorithm, the homogeneous one is tackled expanding the unknown solution in terms of Bessel functions of first and second kinds (Manna & Vacca 1999).

We recall that since the velocity and pressure are decoupled from each other, the space discretization for velocity and pressure can be chosen independently, and they do not need to satisfy the Babuska–Brezzi condition (Shen 1996). Thus we have used equal-order trigonometric and Chebyshev polynomials for both velocity and pressure. The pressure Poisson equation is solved with homogeneous Neumann boundary conditions on $p^n - p^{n-1}$. Convergence properties of the Navier–Stokes kernel with exponential rate of the error decay can be found in Manna & Vacca (1999).

For practical reasons, the Taylor–Couette flow problem described in § 2 is more efficiently represented on a computational domain of finite size, defined in terms of four characteristic length scales, namely L_z, L_θ, R_i, R_o. While the inner and outer radii suffice to characterize the annular geometry in the radial direction, the axial extension has to be defined so that L_z/S is much larger than one. In practice this is difficult in both experimental and numerical studies because perturbations affecting to some extent the fundamental flow features are unfortunately unavoidable. While in experimental set-ups the presence of endwalls induces side effects that have been shown to have an impact on the cell pattern generation (Coles 1965), in numerical studies axial periodicity can be exactly imposed so that the only induced errors pertain to the physical size (axial extension) of the computational domain. With a finite axial length L_z, the most important issue to address concerns the number of coherent large -scale structures that can be properly accommodated within L_z and their impact on the collected statistical data. On the other hand, the azimuthal length L_θ, referred to the mean radius, can be exactly specified equal to $L_\theta = \pi(1+\eta)/(1-\eta)S$. On a finite-sized computational domain a smaller value can be adopted with a criterion similar to the one considered to define the axial length L_z. Details concerning the definition of the computational domain size, along with a grid convergence study, are provided in the Appendix.

Unless otherwise stated all computations have been performed with dimensionless axial and azimuthal lengths equal to $\ell_z = 4$ and $\ell_\theta = \pi/9(1+\eta)/(1-\eta)$. Likewise, the computational domain has been discretized with four subdomains, each of which have 64, 14 and 256 modes in the axial, radial and azimuthal directions, respectively. The radial distribution of subdomain widths in the radial direction has been devised to enhance the wall-layer resolution; the four subdomains' radial width distribution is as follows: 1/6, 1/3, 1/3, 1/6. The time step is set equal to

2.5×10^{-2} and 1.25×10^{-2} dimensionless units, for the $Ta = 1000$ and $Ta = 1500$ cases, respectively. Each simulation is started, destabilizing the velocity distribution given in (2.3) with a small-sized perturbation imposed on the velocity vector field in the Fourier-transformed space. The dimensionless amplitude of the perturbation applied to the first three modes, in both the axial and azimuthal directions, is typically set to 0.05.

4. Results

The dimensionless torque exerted on the inner cylinder is defined in terms of the following coefficient:

$$C_\tau = \overline{\tau}_{r\theta,\mathrm{i}}, \tag{4.1}$$

in which $\overline{\tau}_{r\theta,\mathrm{i}}$ is the dimensionless azimuthal component of the shear stress,

$$\overline{\tau}_{r\theta} = -\frac{1}{Ta}\left(\frac{\mathrm{d}\overline{w}}{\mathrm{d}r} - \frac{\overline{w}}{r}\right), \tag{4.2}$$

at the inner wall. In what follows we shall denote with an overbar the time- and space-averaged quantities over the two homogeneous directions z and θ and with a prime the perturbations from the averaged quantities. Numerical data have been computed, collecting statistics over a time span typically of order 3×10^3 dimensionless time units. With an eddy turnover time of order 70 units, the sample size has been fixed to 50 independent realizations, having discarded the initial transient.

We begin the analysis giving in table 2 the computed values of torque coefficient C_τ for the values of Ta and Re reported in table 1, together with the experimental data of Yamada (1962*b*). The agreement is good, within a 5–10 % difference margin.

The same table presents the torque coefficients C_τ divided by the corresponding circular Couette values, computed by means of the equation

$$C_{\tau c} = \frac{1}{Ta}\frac{1}{\eta(1+\eta)}, \tag{4.3}$$

obtained by replacing (2.1) in (4.1) and (4.2). For ease of reading the torque coefficient computed in absence of any axial pressure gradient is termed $C_{\tau 0}$.

With reference to the $C_\tau/C_{\tau c}$ columns of table 2 we note that while for $Ta = 1000$ the SPF regime is recovered already for $Re = 100$, for the $Ta = 1500$ case this reverse transition process takes place at $Re > 200$. The $C_\tau/C_{\tau 0}$ data demonstrate the gradual reduction of the torque coefficient with Re as consequence of the axial pressure gradient. This gradual process indicates that large-scale coherent structures persist in the annular gap before being killed by the axial flow. This destruction phenomenon occurs through a multiple-scale interaction, as suggested by the velocity component spectra and correlations, reported later on.

Again table 2 shows the values of the resistance coefficients λ defined as

$$\lambda = 4\,\frac{\Delta p}{\ell_z}\frac{Ta^2}{Re^2}, \tag{4.4}$$

in which $\Delta p/\ell_z$ is the mean pressure gradient,

$$\frac{\Delta p}{\ell_z} = 2\,\frac{\overline{\tau}_{rz,o} - \overline{\tau}_{rz,\mathrm{i}}\eta}{1+\eta}, \tag{4.5}$$

	$Ta = 1000$							$Ta = 1500$						
Re	DNS	$C_\tau \times 10^3$ Experiment	Δ (%)	$C_\tau/C_{\tau c}$ DNS	$C_\tau/C_{\tau 0}$ DNS	λ DNS	λ/λ_p DNS	DNS	$C_\tau \times 10^3$ Experiment	Δ (%)	$C_\tau/C_{\tau c}$ DNS	$C_\tau/C_{\tau 0}$ DNS	λ DNS	λ/λ_p DNS
0	2.38	2.45	−2.82	2.31	1.00	–	–	2.03	2.02	0.69	2.96	1.00	–	–
50	2.08	2.21	−5.93	2.02	0.87	0.99	1.04	1.99	1.98	0.64	2.90	0.98	1.03	1.07
100	1.03	–	–	1.00	0.43	0.48	1.00	1.90	1.95	−2.39	2.77	0.94	0.55	1.14
200	1.03	1.03	0.07	1.00	0.43	0.24	1.00	1.72	1.53	12.73	2.51	0.85	0.28	1.15
400	1.03	1.03	0.07	1.00	0.43	0.12	1.00	0.69	0.70	−1.84	1.00	0.36	0.12	1.00

TABLE 2. Global parameters.

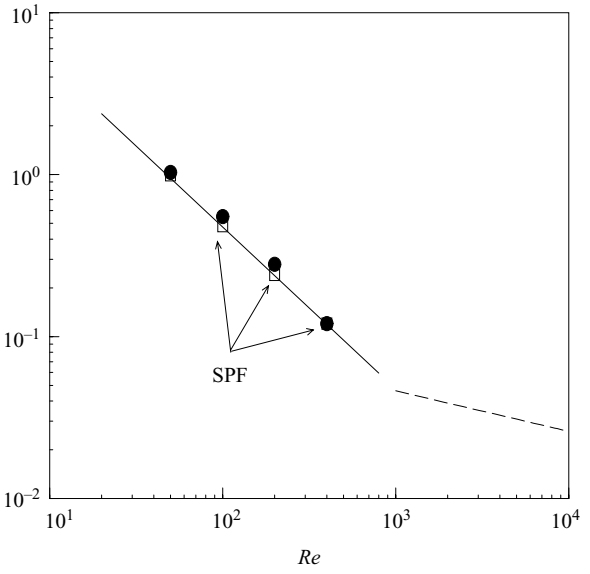

FIGURE 3. Resistance coefficient: Solid line, (4.7); Dashed line, $\lambda = 0.26Re^{-1/4}$; □, $Ta = 1000$; ●, $Ta = 1500$.

with $\overline{\tau}_{rz,\mathrm{i}}$ and $\overline{\tau}_{rz,o}$ the averaged axial components of the shear stress,

$$\overline{\tau}_{rz} = -\frac{1}{Ta}\frac{\mathrm{d}\overline{u}}{\mathrm{d}r}, \tag{4.6}$$

at the inner and outer walls, respectively.

In laminar SPF, the axial velocity $u(r)$ is a unique function of the radial coordinate for given η (see (2.3)), so that replacing (2.3) in (4.6) yields the laminar value

$$\lambda_p = \frac{32}{Re}\left[\frac{(1-\eta)^2}{1+\eta^2+\frac{1-\eta^2}{\log\eta}}\right]. \tag{4.7}$$

For $Ta = 1000$ the axial flow does not affect the axial resistance as demonstrated by the λ/λ_p ratios which remain close to one for all cases. Conversely at $Ta = 1500$, the axial flow rate first induces a moderate λ/λ_p rise which vanishes at $Re = 400$, thus proving that in the $Re = 50$–200 range, the vortical structures do affect the axial shear stress up to the point at which the reverse transition process occurs; i.e. the laminar SPF regime is recovered at $200 \leqslant Re \leqslant 400$. Therefore the Re^{-1} dependence of λ is altered in a small range of Reynolds number, to return to the -1 slope (see figure 3) and to remain so until the laminar to turbulent transition value is achieved, at $Re \sim 10^3$ (Yamada 1962*a*).

From the equilibrium conditions we can easily work out the input power necessary to keep the inner cylinder rotating and to ensure the prescribed flow rate. As concerns the Taylor–Couette problem, the above-mentioned power input, in dimensionless form, is equal to

$$\mathscr{P}_\theta = 2\pi C_\tau \frac{\eta}{1-\eta}\ell_z, \tag{4.8}$$

	$Ta = 1000$				$Ta = 1500$			
Re	$\mathscr{P}_\theta$	$\mathscr{P}_z$	$\mathscr{P}_{tot}$	Δ	$\mathscr{P}_\theta$	$\mathscr{P}_z$	$\mathscr{P}_{tot}$	Δ
0	2.99	0.00	2.99	0 %	2.55	0.00	2.55	0 %
50	2.61	0.04	2.65	−11.4 %	2.50	0.01	2.51	−1.6 %
100	1.29	0.15	1.45	−51.6 %	2.39	0.05	2.44	−4.4 %
200	1.29	0.61	1.90	−36.3 %	2.17	0.21	2.37	−7.1 %
400	1.29	2.44	3.73	24.7 %	0.91	0.72	1.64	−35.9 %

TABLE 3. Input power.

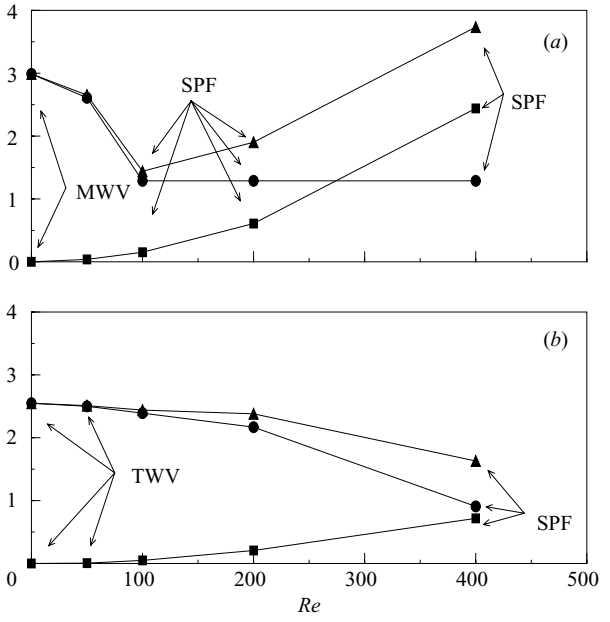

FIGURE 4. Power input: ●, $\mathscr{P}_\theta$; ■, $\mathscr{P}_z$; ▲, $\mathscr{P}_{tot}$. (*a*) $Ta = 1000$; (*b*) $Ta = 1500$.

and for the axial flow

$$\mathscr{P}_z = \frac{\pi}{4}\lambda \frac{Re^3}{Ta^3}\frac{1+\eta}{1-\eta}\ell_z. \tag{4.9}$$

Table 3 and figure 4 give the power split between the azimuthal and axial components along with the overall power $\mathscr{P}_{tot} = \mathscr{P}_\theta + \mathscr{P}_z$ and the percentage variation $\Delta = (\mathscr{P}_{tot} - \mathscr{P}_{\theta,0})/\mathscr{P}_{\theta,0}$, with $\mathscr{P}_{\theta,0}$ the value of $\mathscr{P}_\theta$ obtained for $Re = 0$.

While the power required to drive the axial flow is a monotonically increasing function of the Reynolds number, the azimuthal counterpart decreases before reaching the constant value 1.29 at $Re = 100$ for $Ta = 1000$. The latter represents the Couette value, which can be readily evaluated replacing (4.3) in (4.8). The sum of two contributions reduces up to $Re = 100$ and increases further on. At $Re = 50$ the azimuthal power is nearly twice as much as the steady Couette value (2.61 versus 1.29), and still there is 11 % power reduction, with respect to the power required to drive the azimuthal flow alone, in absence of any axial pressure gradient. The largest power reduction (51.6 %) is attained at $Re = 100$ when the axial flow rate leads to a complete suppression of any crossflow vortical structure under the SPF

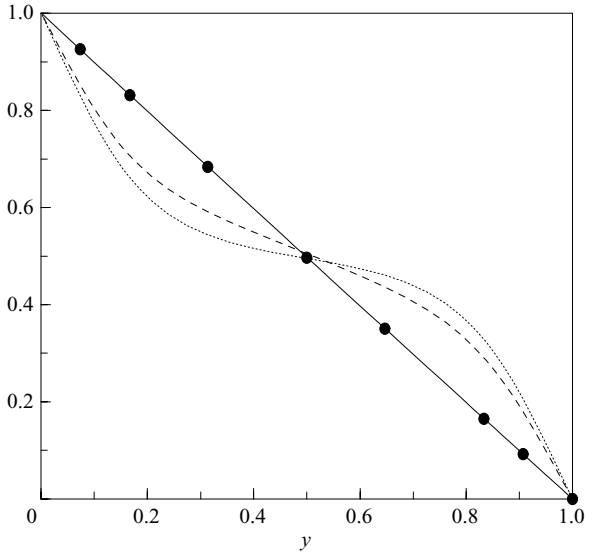

FIGURE 5. Mean azimuthal velocity profiles in outer coordinates at $Ta = 1000$: solid line, Couette; dotted line, $Re = 0$; dashed line, $Re = 50$; ●, $Re = 100$.

regime. Therefore on practical ground it may be inferred that a remarkable torque reduction may be achieved simply superposing a small axial flow rate as to match this optimal Re–Ta pair. Any further increase in the axial flow would lead an overall power increase.

In the $Ta = 1500$ case, the azimuthal contribution is a monotonically decreasing function of Re in the entire range explored. The overall power reduces by 7 % for $Re = 200$, before reaching the SPF value, at $Re = 400$, with an overall power reduction of 36 %. As before, since the SPF condition has been reached, this Ta–Re pair should be considered as the optimal one.

Let us observe that an energy saving in a global sense is achieved only when the power required to drive the combined motion is smaller than the sum of the powers required to drive separately the Taylor–Couette and the axial flows. Thus, the present results provide a precise indication of the state space within which engineering application concerning torque-transferring devices are worthwhile.

In figures 5 and 6 we plot the mean dimensionless azimuthal velocity component $\overline{w}$ as a function of the dimensionless distance from the inner wall y, together with the Couette distribution, for both Taylor numbers. The effects of increasing the Reynolds number are demonstrated through the slope reduction of the velocity profiles at the walls, until the Couette distribution is achieved, and the $C_{\tau c}$ value is recovered. The experiments of Yamada (1962*b*) indicate that a further increase in the Reynolds number induces a corresponding increment of the torque coefficient which eventually will exceed the $C_{\tau 0}$ value. This phenomenon is seen to occur when $Ta \sim Re$, i.e. when the two characteristic velocity scales ΩR_i and U_b, are very close. (For instance for $Ta = 1500$, the condition $C_\tau / C_{\tau 0} = 1$ occurs at $Re \sim 2000$.)

Figures 7 and 8 show, in outer coordinates across the gap width, the dimensionless turbulent kinetic energy profiles defined as $\kappa = 0.5(\overline{u'^2 + v'^2 + w'^2})$, for all (Ta, Re) pairs. For both Taylor numbers the axial flow rate is seen to induce a progressive

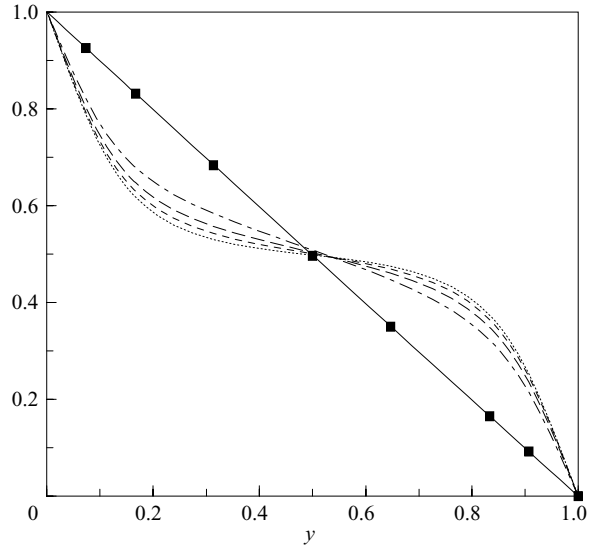

FIGURE 6. Mean azimuthal velocity profiles in outer coordinates at $Ta = 1500$: solid line, Couette; dotted line, $Re = 0$; dashed line, $Re = 50$; long-dashed line, $Re = 100$; dot-dashed line, $Re = 200$; ■, $Re = 400$.

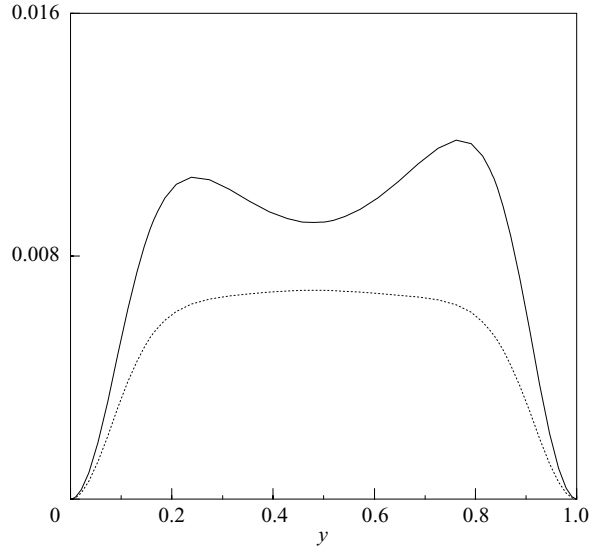

FIGURE 7. Turbulent kinetic energy profiles in outer coordinates at $Ta = 1000$: solid line, $Re = 0$; dotted line, $Re = 50$.

reduction in the turbulent intensities accompanied by a flattening of the profiles in the gap core as Re is increased.

We now turn to the time- and space-averaged azimuthal component of the momentum equations (3.1), which reduces to

$$-[\overline{v'w'} + F(r)] + \overline{\tau}_{r\theta}(r) + G(r) = \overline{\tau}_{r\theta,\mathrm{i}}, \tag{4.10}$$

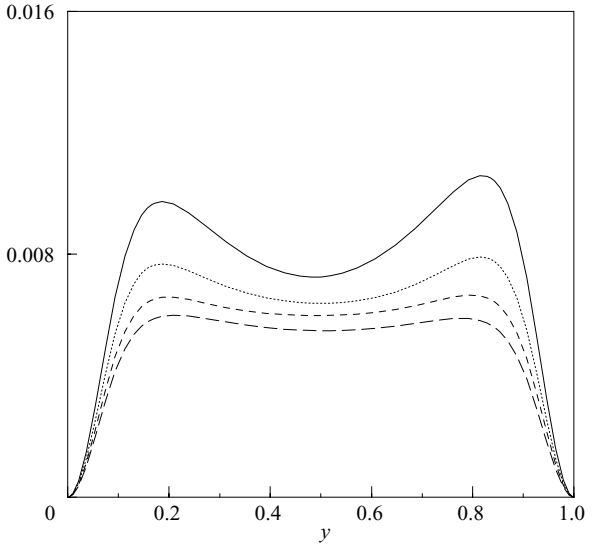

FIGURE 8. Turbulent kinetic energy profiles in outer coordinates at $Ta = 1500$: solid line, $Re = 0$; dotted line, $Re = 50$; dashed line, $Re = 100$; long-dashed line, $Re = 200$.

with

$$F(r) = 2\int_{\eta/(1-\eta)}^{r} \frac{\overline{v'w'}}{r}\mathrm{d}r, \quad G(r) = \frac{2}{Ta}\left(\frac{\overline{w}}{r} - \frac{1-\eta}{\eta}\right). \tag{4.11}$$

In the above equations the F and G functions represent the convective and diffusive terms arising from the cylindrical coordinate formulation, i.e. curvature effects. Note that for $r \to \infty$ ($\eta \to 1$), both the F and G terms vanish and the plane case, with a constant overall stress distribution, is recovered. Figures 9 and 10 show the turbulent (sum of the first and second terms on the left-hand side of (4.10)) and the viscous (sum of the third and fourth terms on the left-hand side of (4.10)) shear stresses, divided by $\overline{\tau}_{r\theta,\mathrm{i}}$, across the gap. In the core region, the increase in the axial Reynolds number induces an appreciable reduction of the turbulent part accompanied by a corresponding increase of the viscous one. In all cases the volume-averaged turbulent shear stress is comparable in magnitude with the viscous one.

To have a deeper insight into the radial distribution of the dissipated power we analyse the individual contributions:

$$\mathscr{P}_{tot} = \mathscr{P}_t + \mathscr{P}_v, \tag{4.12}$$

where $\mathscr{P}_t$ and $\mathscr{P}_v$ respectively denote the turbulent and viscous parts, given by

$$\mathscr{P}_t = -2\pi\ell_z \int_{\eta/(1-\eta)}^{1/(1-\eta)} \left(\overline{u'v'}\frac{\mathrm{d}\overline{u}}{\mathrm{d}r} + \overline{v'w'}\frac{\mathrm{d}\overline{w}}{\mathrm{d}r} - \overline{v'w'}\frac{\overline{w}}{r}\right) r\,\mathrm{d}r, \tag{4.13}$$

$$\mathscr{P}_v = \frac{2\pi}{Ta}\ell_z \int_{\eta/(1-\eta)}^{1/(1-\eta)} \left(\left(r\frac{\mathrm{d}}{\mathrm{d}r}\left(\frac{\overline{w}}{r}\right)\right)^2 + \left(\frac{\mathrm{d}\overline{u}}{\mathrm{d}r}\right)^2\right) r\,\mathrm{d}r. \tag{4.14}$$

Equations (4.13) and (4.14) follow directly from the kinetic energy of the mean flow integrated across the dimensionless volume $\mathscr{V} = \pi\ell_z(1+\eta)/(1-\eta)$, with some algebra, accounting for the homogeneity of the flow field in the axial and azimuthal directions. Figures 11 and 12 present the radial distribution of the terms appearing in integrals (4.13) and (4.14) normalized with the input power of the SPF flow, per

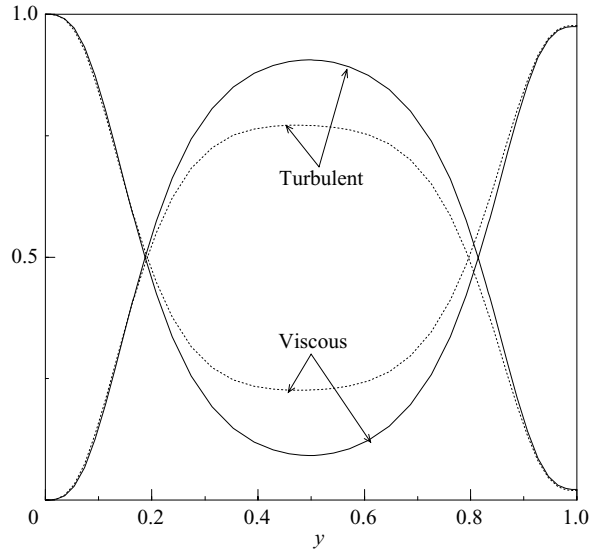

FIGURE 9. Viscous and turbulent shear stress profiles in outer coordinates at $Ta = 1000$: solid line, $Re = 0$; dotted line, $Re = 50$.

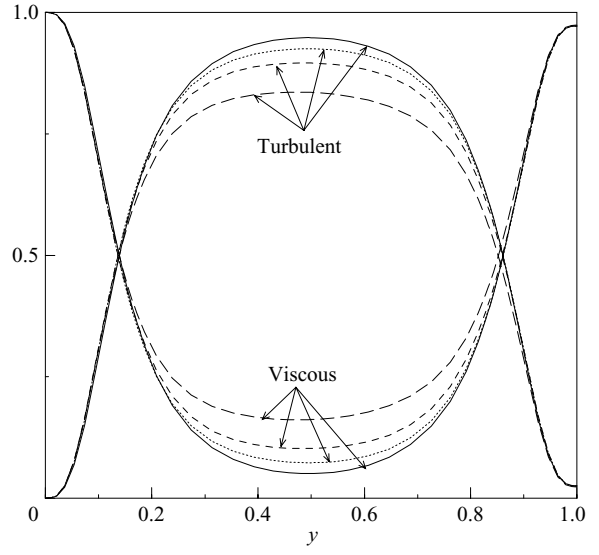

FIGURE 10. Viscous and turbulent shear stress profiles in outer coordinates at $Ta = 1500$: solid line, $Re = 0$; dotted line, $Re = 50$; dashed line, $Re = 100$; long-dashed line $Re = 200$.

unit volume. The viscous contributions, which are obviously largest in the wall layer, drop below the turbulent value in the region $0.2 < y < 0.8$ in the $Ta = 1000$ case, while for $Ta = 1500$ this region is wider, i.e. $0.15 < y < 0.85$. The effects of Reynolds number essentially consist of fuller turbulent dissipation profiles attained through a reduction of the wall-layer peaks and the simultaneous increase of the core values. In the $Ta = 1500$ case, the viscous contribution is negligible in a region of the annular gap representing 40 % of the gap itself.

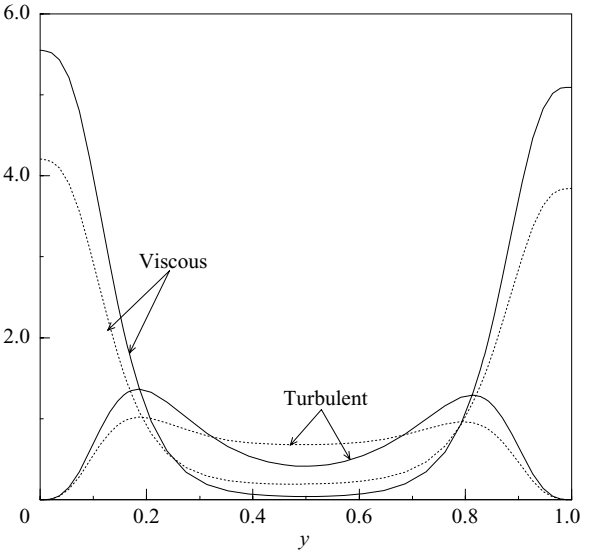

FIGURE 11. Viscous and turbulent dissipation in outer coordinates at $Ta = 1000$: solid line, $Re = 0$; dotted line, $Re = 50$.

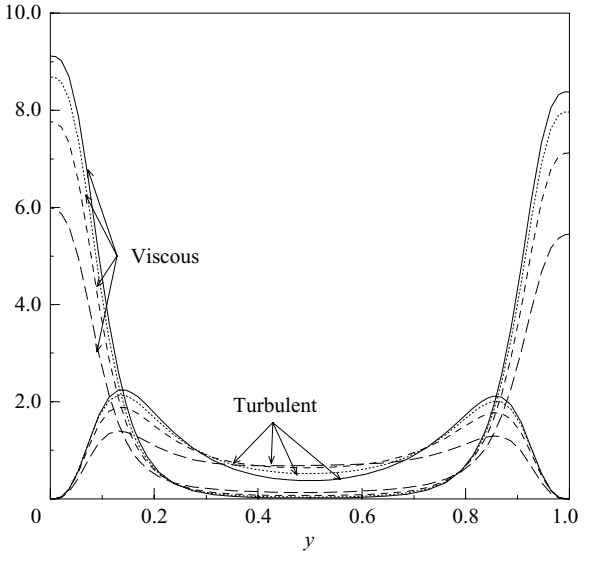

FIGURE 12. Viscous and turbulent dissipation in outer coordinates at $Ta = 1500$: solid line, $Re = 0$; dotted line, $Re = 50$; dashed line, $Re = 100$; long-dashed line, $Re = 200$.

Figures 13–16 depict one-dimensional power spectra of all velocity components in wavenumber space in both the azimuthal ($k_\theta = 2\pi k/\ell_\theta$) and axial ($k_z = 2\pi k/\ell_z$) directions, at $y = 0.11$ for all (Ta, Re) pairs. The spectra of the axial and azimuthal velocities in the θ direction, given in figure 13, are characterized by an interesting crossover point occurring at $k_\theta^\star \sim 1.5$. For $k_\theta < k_\theta^\star$, i.e. at low frequencies, the axial flow rate is observed to induce some energy reduction for both axial and azimuthal fluctuating-velocity components, while the opposite is true for $k_\theta > k_\theta^\star$. The radial component instead undergoes an increase at all azimuthal wavenumbers. These results

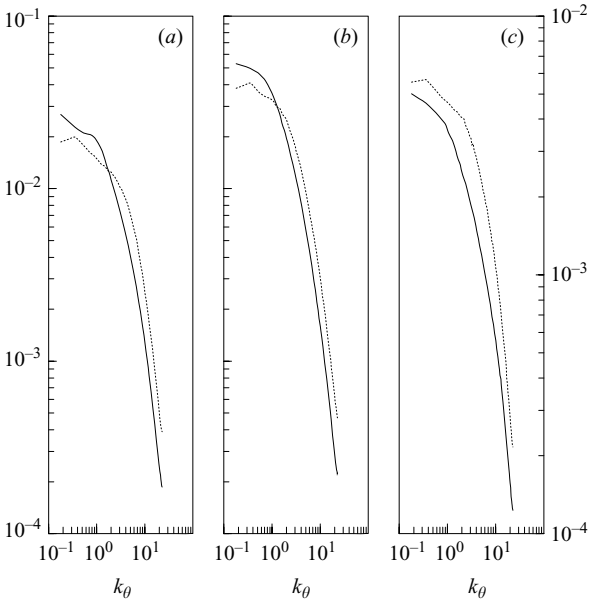

FIGURE 13. Velocity power spectra in θ direction at $Ta = 1000$: (*a*) z component, (*b*) θ component, (*c*) r component; solid line, $Re = 0$; dotted line, $Re = 50$.

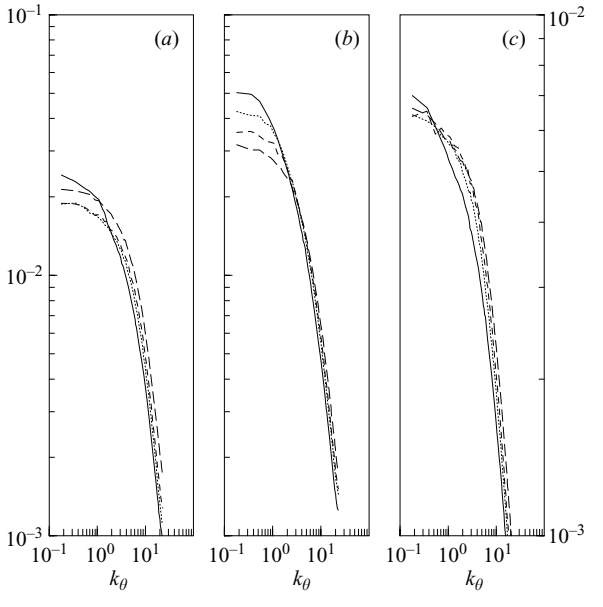

FIGURE 14. Velocity power spectra in θ direction at $Ta = 1500$: (*a*) z component, (*b*) θ component, (*c*) r component; solid line, $Re = 0$; dotted line, $Re = 50$; dashed line, $Re = 100$; long-dashed line, $Re = 200$.

are confirmed at other radial locations (results not shown herein). Because of the radial inhomogeneity the spectra are r dependent, and therefore a local direct energy transfer from the large scales to the small scales cannot be inferred by simple means. However, small scales appear to have increased their energy content, a counter-intuitive

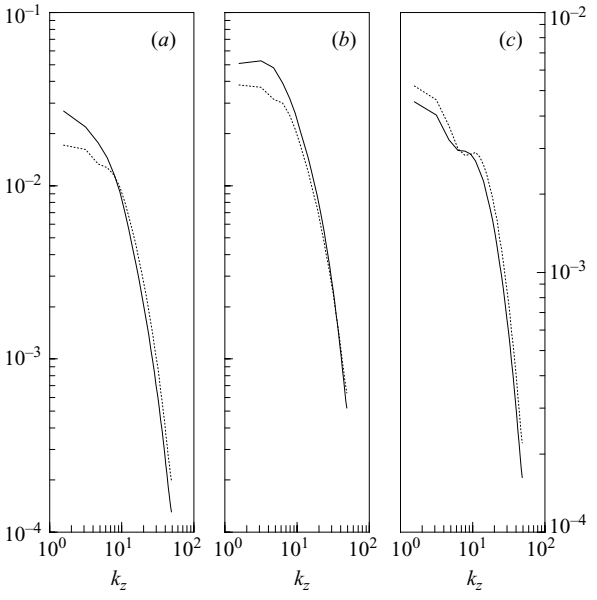

FIGURE 15. Velocity power spectra in z direction at $Ta = 1000$: (a) z component, (b) θ component, (c) r component; solid line, $Re = 0$; dotted line, $Re = 50$.

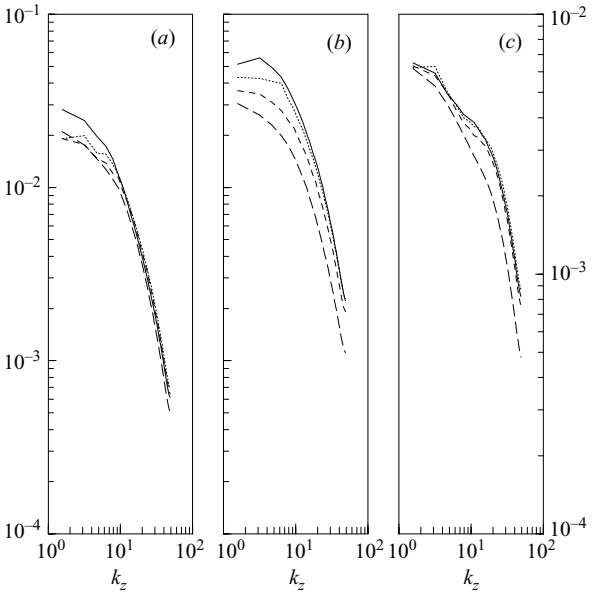

FIGURE 16. Velocity power spectra in z direction at $Ta = 1500$: (a) z component, (b) θ component, (c) r component; solid line, $Re = 0$; dotted line, $Re = 50$; dashed line, $Re = 100$; long-dashed line, $Re = 200$.

event, in a global energy-decreasing context. Similar results obtained in other drag-reducing flow problems have already been reported (see for instance Quadrio & Sibilla 2000). At $Ta = 1500$ (see figure 14) the aforementioned crossover points and the associated large-/small-scale modifications are seen to exist for all fluctuating-velocity

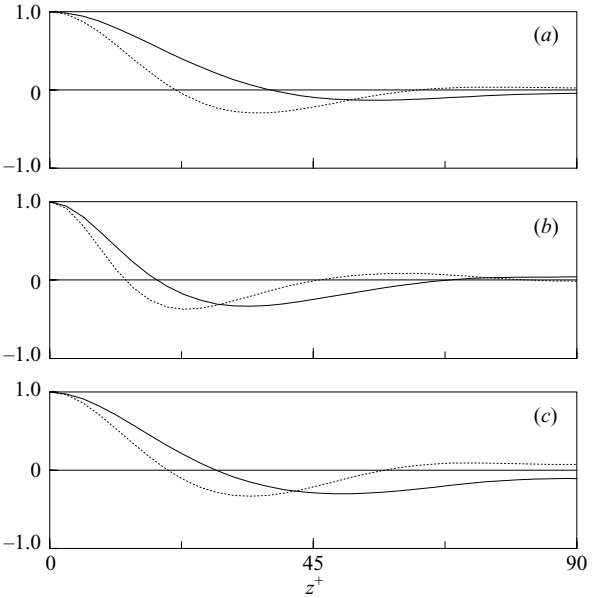

FIGURE 17. Velocity spatial correlation in z direction in inner coordinates at $Ta = 1000$: (a) z component, (b) r component, (c) θ component; solid line, $Re = 0$; dotted line, $Re = 50$.

components. The power spectra in the z direction, representing the counterparts of figures 13 and 14, are given in figures 15 and 16. With the exception of the z component at $Ta = 1000$, exhibiting a crossover point at $k_z^\star \sim 8$, all distributions are characterized by a uniform reduction at all wavenumbers when the axial pressure gradient is imposed.

Comparing the spectra reported in figures 13 and 14 with the corresponding ones of figures 15 and 16 we can infer that the torque reduction is associated with a peculiar modification of the energy-containing structures, as the axial flow rate is increased. The modification consists in a spectral energy gain (loss) in the small (large) scales, in the azimuthal direction, while in the axial direction energy is just lost. Therefore turbulent structures undergo remarkable changes of different nature in z and θ directions, as a consequence of the axial mean shear. Eventually the turbulent structures will not survive the axial mean shear, and reverse transition will occur. Figures 17–20 present the two-point velocity correlations R_{uu}, R_{vv}, R_{ww} in the axial and azimuthal directions at $y = 0.11$ ($y^+ \sim 5$) with and without axial flow, in inner coordinates. For both Taylor numbers the axial pressure gradient induces an appreciable reduction in the axial direction of the characteristic length scale of the coherent structures, defined by twice the separation distance at which the minimum of R_{ww} occurs. In the azimuthal direction the effects of Re consist in a reduction of the zero point. Also the Taylor microscales, in z and θ directions, appear to have reduced in size. To substantiate the above results we show in figures 21 and 22 a single realization of the radial vorticity fluctuations in the θ–z plane in inner coordinates at $y^+ = 5$, for $Ta = 1000$ and $Ta = 1500$, respectively. The most visible effect of the imposed pressure gradient is the progressive tilting in the axial direction z of the elongated wall structures which are aligned with the θ axis at $Re = 0$. Simultaneously there is an appreciable reduction in width of the coherent structures with Re, which is consistent with the two-point correlations of the w' velocity in the z direction.

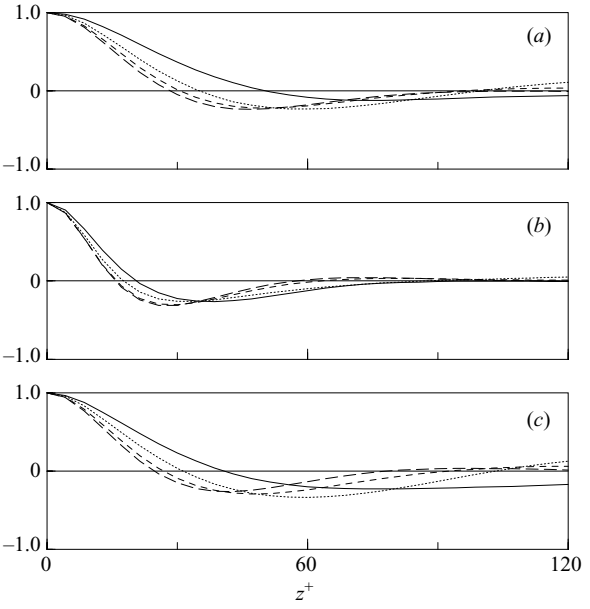

FIGURE 18. Velocity spatial correlation in z direction in inner coordinates at $Ta = 1500$: (a) z component, (b) r component, (c) θ component; solid line, $Re = 0$; dotted line, $Re = 50$; dashed line, $Re = 100$; long-dashed line $Re = 200$.

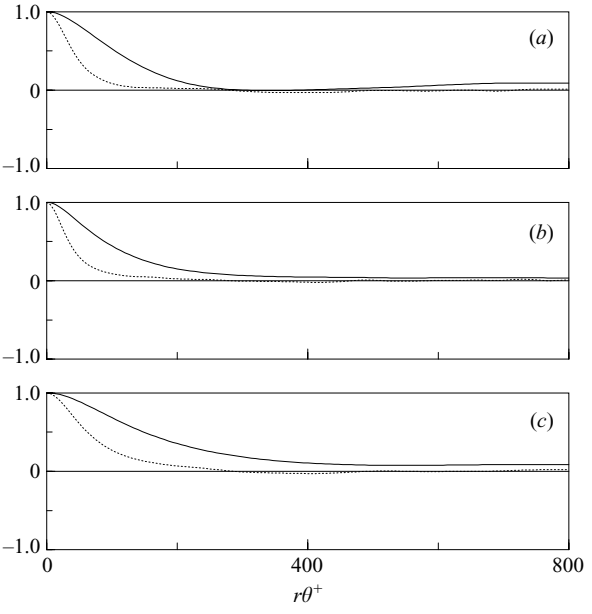

FIGURE 19. Velocity spatial correlation in θ direction in inner coordinates at $Ta = 1000$: (a) z component, (b) r component, (c) θ component; solid line, $Re = 0$; dotted line, $Re = 50$.

Indeed owing to the presence of a moderate tilting, the correlation functions along two orthogonal directions should be simultaneously analysed to characterize the modification occurring to the wall structures.

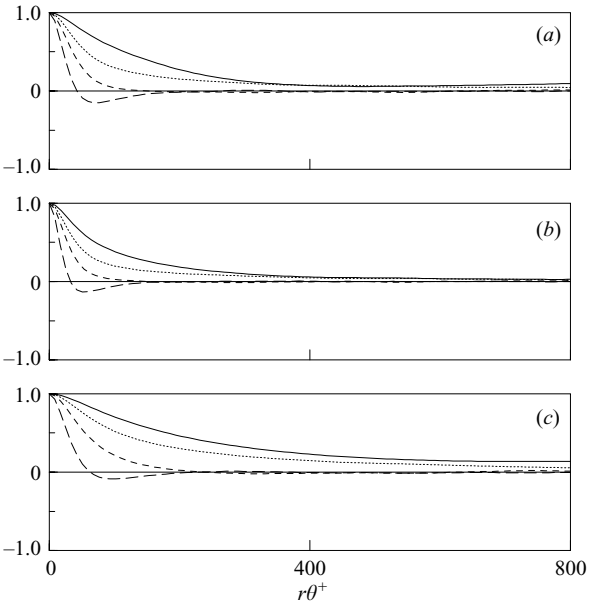

FIGURE 20. Velocity spatial correlation in θ direction in inner coordinates at $Ta = 1500$: (a) z component, (b) r component, (c) θ component; solid line, $Re = 0$; dotted line, $Re = 50$; dashed line, $Re = 100$; long-dashed line, $Re = 200$.

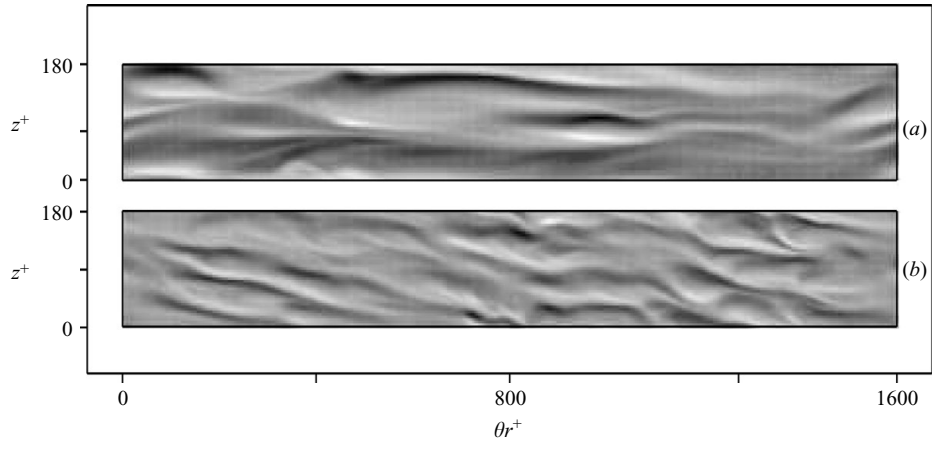

FIGURE 21. Instantaneous shaded map of $\omega_r'^+$ in the θ–z plane in inner coordinates at $y^+ = 5$ ($Ta = 1000$): (a) $Re = 0$, (b) $Re = 50$.

5. Conclusions

The study has dealt with the flow phenomena occurring in a Taylor–Couette arrangement, with a rotating inner cylinder and a fixed outer one, when a steady axial pressure gradient of moderate intensity is imposed. The geometry is characterized by a cylinder radii ratio equal to 0.98, for which extensive experimental data are available. Flow features within the annulus have been investigated by numerical means, that is through space and time integration of the unsteady Navier–Stokes equations, written in cylindrical coordinates, in velocity and pressure formulation. Spatial discretization

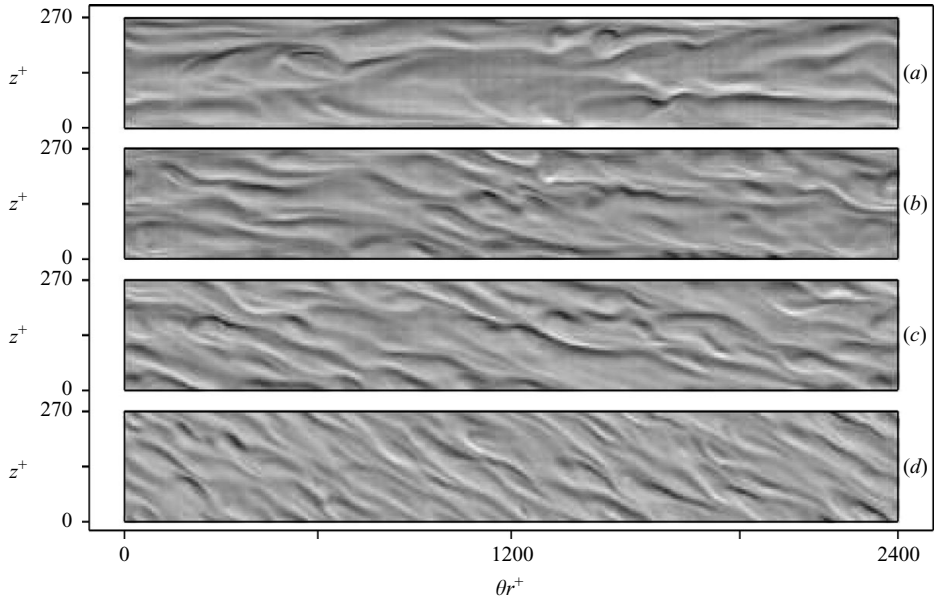

FIGURE 22. Instantaneous shaded map of $\omega_r'^+$ in the θ–z plane in inner coordinates at $y^+ = 5$ ($Ta = 1500$): (*a*) $Re = 0$, (*b*) $Re = 50$, (*c*) $Re = 100$, (*d*) $Re = 200$.

has been performed with a spectral Chebyshev algorithm for the inhomogeneous (radial) direction and blended Fourier decomposition for the homogeneous (axial and azimuthal) ones. Space and time discretization parameters are chosen in order to resolve all scales of motion, so that neither temporal nor spatial filtering is required (DNS). The results, obtained by processing a set of statistically independent data, have been used to investigate the torque reduction occurring in a well-defined region of the Taylor and Reynolds numbers envelope. This phenomenon, already experimentally observed through a global parameter study, has been confirmed by the present work. The analysis of the three-dimensional flow field has been carried out with the help of the radial distributions of the first and second order moments of the velocity fluctuations. The axial pressure gradient is seen to induce a progressive decrease and flattening of the turbulent kinetic energy profiles. Likewise the turbulent shear stress and turbulent dissipation also show a similar trend. The most important changes of the large-scale coherent structures occurring in the torque-reducing regimes have been described in terms of one-dimensional spectra of the velocity component in wavenumber space. In the azimuthal direction, at low wavenumbers the pressure gradient has been documented to induce some energy reduction for both the axial and azimuthal fluctuating-velocity components, while at higher wavenumbers an increase is observed. The radial component instead undergoes an increase at all azimuthal wavenumbers. On the other hand, in the axial direction all distributions are characterized by a uniform reduction at all wavenumbers when the axial pressure gradient is imposed. Therefore it can be inferred that the torque reduction is associated with a peculiar modification of the large-scale coherent structures, as the axial flow rate is increased. The modification consists in a spectral energy gain (loss) at the small (large) scales in the azimuthal direction, while in the axial direction energy is just lost. Indeed turbulent structures are differently modified in the axial and azimuthal directions as a consequence of the axial mean shear. The analysis of two-point velocity

		$Re = 0$		$Re = 50$	
ℓ_z	N_z	$C_\tau \times 10^3$	Δ %	$C_\tau \times 10^3$	Δ %
4	64	2.381	−2.532	2.143	0.920
5	80	2.422	−0.844	2.094	−1.379
6	96	2.453	0.422	2.123	0
7	112	2.443	0	2.124	0.049
8	128	2.443	0	2.123	0

TABLE 4. Effects of the axial length of the computational domain; $N_\theta = 256$, and $N_r = N_p \times N_{sub} = 14 \times 4 = 56$.

correlation functions shows that the axial pressure gradient induces an appreciable reduction of the characteristic length scale of the coherent structures. The power required to drive the overall flow is seen to considerably reduce compared to the power necessary to drive the Taylor–Couette flow alone.

The authors are grateful to Professor Jim Wallace of the University of Maryland for the useful discussions and for reading the manuscript.

Appendix. Box size and accuracy check

To ascertain the correctness of the axial length ℓ_z we have compared in table 4 a few simulations carried out with different lengths, viz. $\ell_z = 4, 5, 6, 7, 8$, for the $(Ta, Re) = (1000, 0)$ and $(Ta, Re) = (1000, 50)$ pairs, in terms of torque coefficient. The achievements of the study are applicable to the $Ta = 1500$ cases, provided the spatial resolution is sufficient to resolve the smallest scales which, as a consequence of the Taylor number increase, have reduced in size. We shall return to this point later on.

As already stated in § 3, the baseline configuration of the computational domain consists of four subdomains, each with 64, 14 and 256 modes in the axial, radial and azimuthal directions, respectively. A grid refinement study detailed later on will demonstrate the grid size adequacy.

When the axial length was increased, the number of points in the z direction was increased too, in order to maintain the same spatial resolution, while the azimuthal and radial resolutions were kept unchanged (i.e. $N_\theta = 256$ and $N_r = N_p \times N_{sub} = 14 \times 4 = 56$). The angular width $\beta = \ell_\theta / r$, fixed to $2\pi/9$, will be detailed later on. In both cases ($Re = 0$ and $Re = 50$) the torque coefficients showed negligible variations, compared with the $\ell_z = 8$ computations, assumed as reference data, with a maximum percentage error of 2.53 and 1.38, respectively. In figure 23 the two-point correlation coefficients in the axial direction for all velocity components, at $y = 0.11$, are shown, for $Ta = 1000$: (a–c) $Re = 0$ and (d–f) $Re = 50$.

While in the $(Ta, Re) = (1000, 0)$ case some differences are visible, particularly for the axial and azimuthal components, in the $(Ta, Re) = (1000, 50)$ simulations all correlations show a more than satisfactory collapse. In view of the considerable overall number of points of the shortest domain ($\ell_z = 4$, $N_{tot} = 0.92 \times 10^6$), and of the negligible variations in the global data reported in table 4, this configuration has been considered acceptable and retained for all simulations.

The above procedure has been applied to assess the azimuthal length of the computational domain which has been varied by changing its angular width β in

		$Re=0$		$Re=50$	
β	N_θ	$C\tau\times10^3$	Δ %	$C\tau\times10^3$	Δ %
6	384	2.381	0	2.079	0
9	256	2.381	0	2.082	0.149
12	192	2.371	−0.433	2.082	0.149

TABLE 5. Effects of the azimuthal length of the computational domain; $N_z=64$ and $N_r=N_p\times N_{sub}=14\times4=56$.

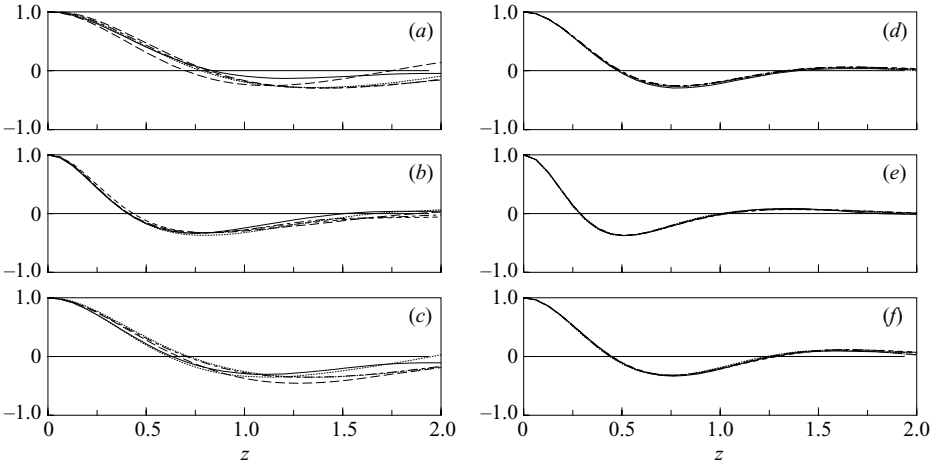

FIGURE 23. Velocity spatial correlations in the z direction at $Ta=1000$: (a) z component, $Re=0$; (b) r component, $Re=0$; (c) θ component, $Re=0$; (d) z component, $Re=50$; (e) r component, $Re=50$; (f) θ component, $Re=50$; solid line, $\ell_z=4$; dotted lines, $\ell_z=5$; dashed line, $\ell_z=6$; long-dashed line, $\ell_z=7$; dot-dashed line, $\ell_z=8$.

the range $2\pi/12$–$2\pi/6$. Table 5, which is the counterpart of table 4, reports the torque coefficients, together with the grid resolution and the percentage errors. Again, the resolution in θ direction is kept constant while increasing the azimuthal length, maintaining the axial and radial number of points unchanged (i.e. $N_z=64$ and $N_r=N_p\times N_{sub}=14\times4=56$). The length ℓ_z has been fixed to 4.

In figure 24(a–c) the two-point correlation coefficients in the azimuthal direction for all velocity components, at $y=0.11$, are given, for both $(Ta, Re)=(1000, 0)$ and $(Ta, Re)=(1000, 50)$ pairs.

Both global and local data confirm the fact that a box size in the azimuthal direction of $2\pi/9$ is sufficient to accommodate the largest flow structures controlling the flow dynamics.

A grid refinement study has been carried out separately, increasing the grid size in the homogeneous directions z and θ for a given box dimension (i.e. $\ell_z=4$ and $\beta=2\pi/9$). For the sake of keeping down the computational cost, the number of modes has been increased by a factor 1.5, yielding the results of table 6. Data show no appreciable changes in the global statistical quantities of interest. (The largest difference is less than 1.2 %.)

As a further proof of the appropriate spatial resolution, one-dimensional power spectra of all velocity components in outer coordinates versus k_θ and k_z, at $y=0.11$, are given in figure 25. The considerable increase in the number of points (of

N_z	$N_p \times N_{sub}$	N_θ	$N_{tot} \times 10^{-6}$	$C\tau \times 10^3$
64	14×4	256	0.918	2.381
64	14×4	350	1.254	2.412
96	14×4	256	1.376	2.368

TABLE 6. Grid refinement study.

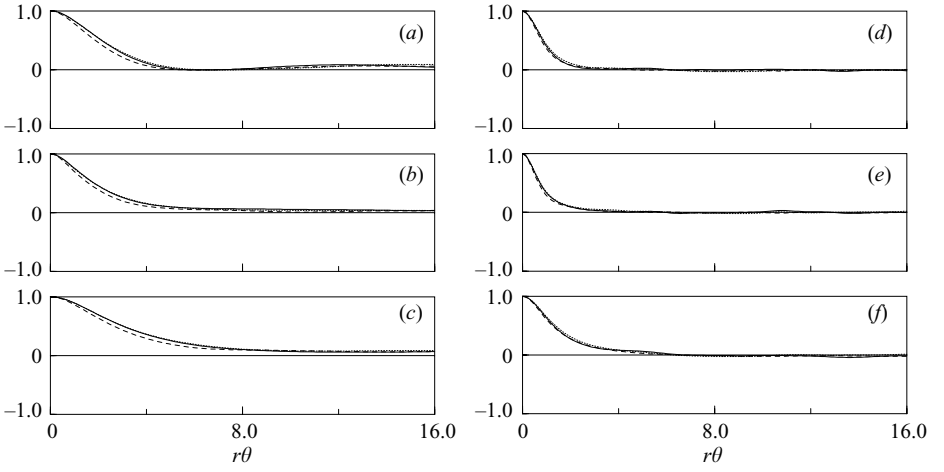

FIGURE 24. Velocity spatial correlations in the azimuthal direction at $Ta = 1000$ (a) z component, $Re = 0$; (b) r component, $Re = 0$; (c) θ component, $Re = 0$; (d) z component, $Re = 50$; (e) r component, $Re = 50$; (f) θ component $Re = 50$; solid line, $\beta = 12$; dotted line, $\beta = 9$; dashed line, $\beta = 6$.

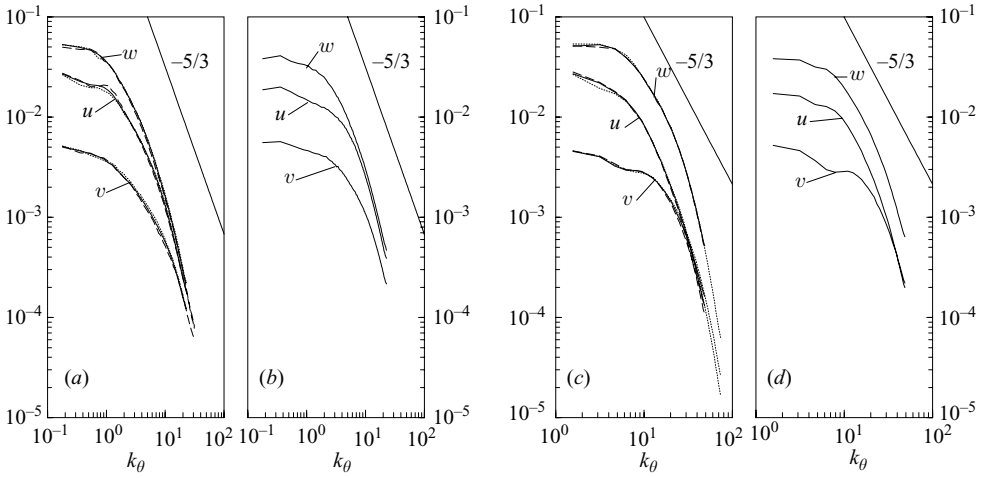

FIGURE 25. Velocity power spectra at $Ta = 1000$. In θ direction: (a) $Re = 0$, (b) $Re = 50$; in z direction: (c) $Re = 0$, (d) $Re = 50$; solid line, $(64 \times 14 \times 256) \times 4$; dotted line, $(96 \times 14 \times 256) \times 4$; long-dashed line, $(64 \times 14 \times 350) \times 4$.

several hundred thousand points) does not produce appreciable differences at all wavenumbers. Moreover, spectra are smooth for all grids, a consequence of the appropriate sample size, and full, despite the absence of an inertial subrange. The lack of any pile-up at the highest wavenumbers ensures that all scales of motion

are correctly resolved, even on the coarse grid, so that the simulation can safely be termed a DNS. Power spectra at $Ta = 1500$ are similar to those presented in figure 25 and thus have been omitted.

REFERENCES

Andereck, C. D., Liu, S. S. & Swinney, H. L. 1986 Flow regimes in a circular Couette system with independently rotating cylinder. *J. Fluid Mech.* **164**, 155–183.

Avila, M., Meseguer, A. & Marques, F. 2006 Double Hopf bifurcation in corotating spiral Poiseuille flow. *Phys. Fluids* **18**, 064101.

Becker, K. M. & Kaye, J. 1962 Measurements of adiabatic flow in an annulus with a rotating inner cylinder. *Intl J. Heat Transfer* **84**, 97–105.

Chandrasekhar, S. 1960 The hydrodinamic stability of viscid flow between coaxial cylinder. *Proc. Natl Acad. Sci.* **46** (1), 137–141.

Chandrasekhar, S. 1961 *Hydrodynamic and Hydromagnetic Stability*. Oxford University Press.

Chandrasekhar, S. 1962 The stability of spiral flow between rotating cylinders. *Proc. R. Soc. Lond.* A **265**, 188–197.

Chung, K. C. & Astill, K. N. 1977 Hydrodynamic instability of viscous flow between rotating coaxial cylinders with fully developed axial flow. *J. Fluid Mech.* **81**, 641–655.

Chung, S. Y. & Sung, H. J. 2005 Large-eddy simulation of turbulent flow in a concentric annulus with rotation of an inner cylinder. *Intl J. Heat Fluid Flow* **26**, 191–203.

Coles, D. 1965 Transition in circular Couette flow. *J. Fluid Mech.* **21**, 385–425.

Datta, S. K. 1965 Stability of spiral flow between concentric circular cylinders at low axial Reynolds number. *J. Fluid Mech.* **21** (04), 635–640.

Davey, A. 1965 The growth of Taylor vortices in flow between rotating cylinders. *J. Fluid Mech.* **14**, 336–368.

Elliott, L. 1973 Stability of a viscous fluid between rotating cylinders with axial flow and pressure gradient round the cylinders. *Phys. Fluids* **16**, 577–580.

Escudier, M. P. & Gouldson, I. W. 1995 Concentric annular flow with centerbody rotation of a newtonian and non–newtonian and a shear thinning liquid. *Intl J. Heat Fluid Flow* **38**, 156–162.

Fenstermacher, P. R., Swinney, H. L. & Gollub, J. P. 1979 Dynamical instabilities and the transition to chaotic Taylor vortex flow. *J. Fluid Mech.* **94**, 103–129.

Hasoon, M. A. & Martin, B. W. 1977 The stability of viscous axial flow in an annulus with a rotating inner cylinder. *Proc. R. Soc. Lond.* **352** (1670), 351–380.

Heise, M., Hoffmann, Ch., Abshagen, J., Pinter, A., Pfiste, G. & Lucke, M. 2008 Stabilization of domain walls between travelling waves by nonlinear mode coupling in Taylor–Couette flow. *Phys. Rev. Lett.* **100**, 064501.

Hoffmann, Ch., Lucke, M. & Pinter, A. 2004 Spiral vortices and Taylor vortices in the annulus between rotating cylinders and the effect of an axial flow. *Phys. Rev.* E **69**, 056309.

Hughes, T. H. & Reid, W. H. 1968 The stability of spiral flow between rotating cylinders. *Proc. R. Soc. Lond.* A **265**, 57–91.

Hwang, J. Y. & Yang, K. S. 2004 Numerical study of Taylor–Couette flow with an axial flow. *Comp. Fluids* **33**, 97–118.

Joseph, D. C. 1976 *Stability of Fluid Motion*. Springer.

Jung, S. Y. & Sung, H. J. 2006 Characterization of the three-dimensional turbulent layer in a concentric annulus with a rotating inner cylinder. *Phys. Fluids* **18**, 115102–1151013.

van Kan, J. 1986 A second order accurate pressure correction scheme for viscous incompressible flow. *J. Sci. Stat. Comput.* **7**, 870–891.

Kataoka, K., Doi, H. & Komai, T. 1977 Heat/mass transfer in Taylor vortex flow with constant axial flow rates. *Intl J. Heat Mass Transfer* **20**, 57–63.

Kaye, J. & Elgar, E. C. 1958 Modes of adiabatic and adiabatic fluid flow in an annulus with an inner rotating cylinder. *Trans. ASME* **80**, 753–765.

Lueptow, R. M., Docter, A. & Min, K. 1992 Stability of axial flow in an annulus with a rotating inner cylinder. *Phys. Fluids* **4** (11), 2446–2455.

Manna, M. & Vacca, A. 1999 An efficient method for the solution of the incompressible Navier–Stokes equations in cylindrical geometries. *J. Comput. Phys.* **151**, 563–584.

Marcus, P. S. 1984 Simulation of Taylor–Couette flow. Part 2. Numerical results for wavy-vortex flow with one travelling wave. *J. Fluid Mech.* **146**, 65–113.

Moulic, S. G & Yao, L. S. 1996 Taylor–Couette instability of travelling waves with a continuous spectrum. *J. Fluid Mech.* **324**, 181–198.

Ng, B. S. & Turner, E. R. 1982 On the linear stability of spiral flow between rotating cylinders. *Proc. R. Soc. Lond.* A **382** (1782), 83–102.

Nouri, J. M. & Whitelaw, J. H. 1994 Flow of newtonian and non–newtonian fluids in a concentric annulus with rotation of the inner cylinder. *Trans. ASME: J. Fluids Engng* **116**, 821–827.

Orzag, S. A. & Patera, A. T. 1983 Secondary instability of wall bounded shear flows. *J. Fluid Mech.* **128**, 347–385.

di Prima, R. C. 1960 The stability of a viscous fluid between rotating cylinders with an axial flow. *J. Fluid Mech.* **9** (04), 621–631.

di Prima, R. C. 1961 Stability of non-rotationally symmetric disturbances for viscous flow between rotating cylinders. *Phys. Fluids* **4**, 751–755.

di Prima, R. C. & Pridor, A. 1979 The stability of viscous flow between rotating concentric cylinders with an axial flow. *Proc. R. Soc. Lond.* **366** (1727), 553–573.

Quadrio, M. & Sibilla, S. 2000 Numerical simulation of turbulent flow in a pipe oscillating around its axis. *J. Fluid Mech.* **424**, 217–241.

Recktenwald, A., Lucke, M. & Muller, H. W. 1993 Taylor vortex formation in axial through-flow: linear and weakly nonlinear analysis. *Phys. Rev.* E **48**, 4444–4454.

Schroeder, W. & Keller, H. B. 1990 Wavy Taylor–vortex flows via multigrid continuation method. *J. Comput. Phys.* **91**, 197–227.

Schwarz, K. W., Springett, B. E. & Donnelly, R. J. 1964 Modes of instability in spiral flow between rotating cylinders. *J. Fluid Mech.* **20**, 281–289.

Shen, J. 1996 On error estimates of the projection methods for the Navier–Stokes equations: second order schemes. *Math. Comput.* **65** (215), 1039–1065.

Snyder, H. A. 1962 Experiments on the stability of spiral flow at low axial Reynolds numbers. *Proc. R. Soc. Lond.* **265** (1321), 198–214.

Takeuchi, D. I. & Jankowski, D. F. 1981 A numerical and experimental investigation of the stability of spiral Poiseuille flow. *J. Fluid Mech.* **102**, 101–126.

Tsameret, A. & Steinberg, V. 1994 Competing states in a Couette–Taylor system with an axial flow. *Phys. Rev.* E **49** (5), 4077–4087.

Wereley, S. T. & Lueptow, R. M. 1999 Velocity field for Taylor–Couette flow with an axial flow. *Phys. Fluids* **11** (12), 3637–3649.

Yamada, Y. 1962*a* Resistance of a flow through an annulus with an inner rotating cylinder. *Bull. JSME* **5** (18), 302–310.

Yamada, Y. 1962*b* Torque resistance of a flow between rotating co-axial cylinders having an axial flow. *Bull. JSME* **5** (20), 634–642.